Monthly variations of forcing mechanisms of austral summer precipitation in subtropical Argentina

Santiago I. Hurtado, Eduardo A. Agosta, Pablo G. Zaninelli

PII: S0169-8095(23)00006-6

DOI: https://doi.org/10.1016/j.atmosres.2023.106609

Reference: ATMOS 106609

To appear in: *Atmospheric Research*

Please cite this article as: S.I. Hurtado, E.A. Agosta and P.G. Zaninelli, Monthly variations of forcing mechanisms of austral summer precipitation in subtropical Argentina, *Atmospheric Research* (2023), https://doi.org/10.1016/j.atmosres.2023.106609

Monthly variations of forcing mechanisms of austral summer precipitation in subtropical Argentina

Santiago I. Hurtado[a,b,c] , Eduardo A. Agosta[b,c], Pablo G. Zaninelli[d,b,c]

a Instituto de Investigaciones Forestales y Agropecuarias Bariloche (IFAB), INTA-CONICET, San Carlos de Bariloche, Río Negro, Argentina

b Consejo Nacional de Investigaciones Científicas y Técnicas (CONICET)

c Facultad de Ciencias Astronómicas y Geofísicas, Universidad de La Plata, La Plata, Buenos Aires, Argentina

d Instituto de Geociencias (IGEO), Consejo Superior de Investigaciones Científicas (CSIC)-Universidad Complutense de Madrid, Madrid, España UMI3351-IFAECI/CNRS-CONICET-UBA

* Corresponding Author: santiagoh719@gmail.com

Abstract

Summer precipitation is a crucial variable for Subtropical Argentina (STAr) from a social and economic perspective. Monthly forcing mechanism variations of subregional summer precipitation over STAr are studied. Most subregional precipitation anomalies are related to a convection dipole between eastern STAr and the South Atlantic Convergence Zone (SACZ) region. In this sense, wet (dry) conditions in subregions of eastern STAr are associated with anomalous low-level anticyclonic (cyclonic) tropospheric circulation in southeastern Brazil. The anomalies are mainly associated with a teleconnection via Rossby wave train that propagate through the South Pacific, which is link to El Niño Southern Oscillation (ENSO) phenomena in December, to enhanced convection in the western tropical Pacific in January, and to conversion of mean flow kinetic energy in January and February. Also, the anomalous low-level anticyclonic tropospheric circulation in southeastern Brazil (wet conditions in eastern STAr) is related to anomalous Walker cell caused mainly by an active convection core in the western Pacific basin probably owing to the Madden-Julian Oscillation (MJO) phases 6 and 7. In addition, dry (wet) conditions in subregions of southwestern STAr in January and February are associated with an anomalous low-level tropospheric anticyclonic (cyclonic) circulation over Patagonia and the Argentinian Sea. The tropospheric anticyclonic circulation anomaly center in February appears to be generated by vorticity flux convergence owing to a quasi-stationary Rossby wave activity from the previous month (January) that generates positive geopotential height anomalies over Patagonia and surrounding areas.

Key words: Subtropical Argentina, Summer Precipitation, Teleconnection, Rossby Wave, ENSO, Precipitation Dipole

1. Introduction

Subtropical Argentina (STAr) is defined as the region roughly to the north of 34° S and the east of the Andes, over central-northern Argentina (see Fig. 1). Its food and hydroelectric energy productions represent more than 80% of Argentina's gross domestic product, mainly in southern La Plata basin (Magrin et al., 2005, Penalba and Vargas, 2008, Cuya et al., 2013). Both hydroelectric energy production and food production are highly dependent on precipitation and its variability, which makes it a crucial variable to the region. STAr's precipitation regime exhibits a sharp annual cycle with two seasons, a wet season spanning from October to April and a dry season, from May to September (Hurtado et al., 2020). The austral summer (December-February) is the season with the highest precipitation in the annual mean cycle (Hurtado, 2022). Both wet season and summer precipitation are key to STAr as evidenced by the large number of studies in the literature, such as, Rusticucci and

Penalba (2000), Barros et al. (2008), Barreiro (2010), González et al. (2012), Marengo et al. (2012), Cai et al. (2020), Robledo et al. (2020), Díaz et al. (2021), Lavin-Gullon et al. (2021), Hurtado (2022), among others.

Austral summer precipitation in the region presents a sharped zonal gradient ranging from roughly 25-50 mm/month to the west (near the Andes) and 130-170 mm/month to the east (see Fig. 2 upper panels). An exception is a narrow meridionally extended precipitation peak in the northwest called the Yungas jungle which exhibits monthly mean precipitation values around 150-200 mm/month (see Fig. 2 upper panels). The overall monthly precipitation variation coefficient over the region is around 0.6-0.8, with greater variability in the arid western region (see Fig. 2 lower panels).

The leading mode of summer precipitation variability over South America (SA) is a dipole between the South Atlantic Convergence Zone (SACZ) and the eastern STA area (Vera et al., 2006, Junquas et al., 2012). This dipole is associated with a high (low) pressure anomalies in lower tropospheric levels, that enhance moisture convergence (divergence) in eastern STAr and inhibit (enhance) convection in SACZ region (Vera et al., 2006, Ma et al., 2012). The latter tropospheric circulation anomaly pattern is driven by different mechanisms in a variety of time-scales, from sub-monthly to interannual, such as: variations in intensity and frequency of South American Low-Level Jet (SALLJ) events (Montini et al., 2019), sub-monthly Rossby wave trains (Van Der Wiel et al., 2015), remote teleconnections from the Madden-Julian Oscillation (MJO; Álvarez et al., 2016) and from El Niño - Southern Oscillation (ENSO; Hurtado and Agosta, 2021).

On a seasonal scale, the MJO (an eastward propagating organized convection perturbation in the Indian and Pacific tropics) modulates SA precipitation through changes in the Hadley and Walker cells and via Rossby wave train emanation from convection activated over the Indo-Pacific (Álvarez et al., 2016, Grimm, 2019, Schwendike et al., 2021). In turn, the ENSO is by far the major forcing of SA precipitation at interannual time scale (Grimm, 2011). There is a high consensus that in austral spring and early summer (October–December) the ENSO modulates SA precipitation through an extratropical Rossby wave train across the South Pacific that imposes low-level circulation anomalies responsible for the SA precipitation dipole (Cazes-Boezio et al., 2003, Grimm, 2003, Grimm and Zilli, 2009, Tedeschi et al., 2015, Cai et al., 2020, Hurtado and Agosta, 2021, among others). In this sense, El Niño (EN) events are associated with enhanced convection in eastern STAr and inhibited convection in the SACZ, while La Niña (LN) events are associated with the inverse situation (Hurtado and Agosta, 2021).

Most of the previous research works study precipitation in summer as a whole, or compact season, through summer precipitation totals. However, monthly precipitation in STAr shows from null-to-weak monthly co-variability among austral summer months. For example, correlation at a station level among December and January (January and February) precipitation times series ranges -0.35 to 0.46, being for most stations close to zero (see Fig. S1). This is indicative that different forcing mechanisms are driving monthly precipitation variations in the region. Therefore, the present work aims at determining the forcing mechanisms of monthly precipitation variations in subregions of STAr throughout the summer season (from December, January and February, individually). For this purpose the work is organized as follows: first, the data and methods are described in Section 2; secondly, the precipitation variability is clustered into subregions of common inter-annual variability in Section 3.1; thirdly, its monthly forcings are assessed for December, January and February in Section 3.2, 3.3 and 3.4, respectively; and lastly, the conclusions are presented in Section 4.

2. Data and methods

STAr is a region characterized by its climate diversity, with complex orography and low weather station density (Hurtado et al., 2021). Sixty-two rain-gauge stations with monthly data in the period 1979-2018 were used, provided by the Argentine National Meteorological Service (SMN, after its Spanish abbreviation, https://www.smn.gob.ar/. See Table S1 and Figure 1. These rain-gauge stations follow the World Meteorological Organization (WMO) standards and they are part of the WMO Global Telecommunication System (GTS). A thorough quality control analysis to achieve continuous and homogeneous data was performed by Hurtado et al. (2020) and Hurtado et al. (2021). After this analysis, eighteen rain-gauge stations were removed because either their records were not reliable or were not long enough. Besides, three more stations (La Quiaca, #87007, Uspallata, #87405, and Malargüe, #87506) were removed since they are located in areas of very high terrains, presenting particular features that represent local mountain climates.

The commonly used grouping methodologies to define subregions of common co-variability are k-means, Self Organizing Maps, Dendrograms, and Principal Component Analysis (PCA) based methods, among others (examples can be found in: Mills, 1995, Grimm et al., 2000, Carvalho et al., 2016, Roushangar and Alizadeh, 2018, Guntu et al., 2020, among others). These methodologies cluster all the data by forcing every station to be part of a subregion, even if the grouped stations may not have common features. For a region like STAr with low spatial density of rain-gauge stations and low spatial autocorrelation (Hurtado et al., 2020, 2021, Hurtado, 2022), the latter is a problem since a station may have nothing in common with its nearby stations. For example, for 50% of the weather stations, the precipitation variability linearly explained by the nearest station in summer months is less than 31%. Furthermore, less than 25% of the stations present a linearly explained variability over 50%. Therefore to assess the potential clustering of subregions with year-to-year co-variability of monthly precipitation, a method was proposed and computed. The spatial co-variability among stations within a certain subregion j (SR_j, with j = 1, . . . N, where N is the number of subregions obtained for every month) is captured by designing an appropriate monthly precipitation index (PI_j) as defined by Agosta et al. (1999). Every PI_j captures the interannual to multidecadal variability of monthly precipitation within each SR_j (Compagnucci et al., 2002, Agosta and Compagnucci, 2012). Thus, the spatial grouping into a coherent SR_j is based on maximizing the amount of stations used to build the PI_j and keeping correlation coefficients between the PI_j and every station from SR_j higher than 0.75. In doing so, there are some stations that stay unclassified into any SR_j. Other stations, instead, show moderate correlation with a PI_j ($0.5 < Corr < 0.75$) and therefore they are classified into the corresponding SR_j though not included to build the PI_j. Further details of the grouping methodology can be found in the Appendix A.

To explore potential relationships with the observed precipitation and climate variables, some climate indices were used, such as: the C and E indices retrieved from http://www.met.igp.gob.pe/variabclim/indices.html, the traditional ENSO indices (NINO1+2, NINO3, NINO3.4 and NINO4) retrieved from https://www.psl.noaa.gov/data/climateindices/list/, and the Real-time Multivariate index to monitor the MJO (RMM1 and RMM2; Wheeler and Hendon, 2004) retrieved from http://www.bom.gov.au/climate/mjo/graphics/rmm.74toRealtime.txt. The C and E indices are uncorrelated indices obtained from an equatorial Pacific SST PCA developed by Takahashi et al. (2011) which represent the Central Pacific and Eastern Pacific ENSO flavors, respectively. The C index was used to define EN and LN events following the methodology described by Hurtado and Agosta (2021).

Atmospheric variables on a 0.25° latitude-longitude grid from the ECMWF ERA5 reanalysis were used (Hersbach et al., 2018, 2019a,b, 2020). This data-set covers the 1979–to the present period. The reanalysis data consisted in: geopotential height (GH) and wind at 250hPa and 850hPa, mean sea level pressure (MSLP), omega (ω) at 500hPa, and vertically integrated moisture flux (MF) and its divergence. Furthermore, some derived variables were calculated: the potential velocity (CHI) at 250hPa, the wave activity flux (WF Takaya and Nakamura, 2001) at 250hPa, and the GH tendency (dGH/dt) equation from low frequency vorticity flux convergence (Lau and Holopainen, 1984), following the methodology describe in Agosta et al. (2019).

The outgoing long-wave radiation (OLR) data is from the National Center of Atmospheric Research, retrieved from https://psl.noaa.gov/data/gridded/data.interp_OLR.html. It is a gridded data-set with temporal integration on a regular grid of 2.5° latitude ×2.5° longitude (Liebmann and Smith, 1996). To explore the physical mechanisms, monthly composite anomalies of diverse climate variables, and their difference, were done for every set of high ($PI_j > 75^{th}$ percentile) and low ($PI_j < 25^{th}$ percentile) PI_j values (Von Storch and Zwiers, 2002). Anomalies were estimated considering 1981-2010 climatology and were tested using the unequal-variance Student's *t*-test at a significance level $\alpha = .10$ (Moser and Stevens, 1992, Wilks, 2011). All graphics and computations were done using R, in particularly four packages were used: ggplot2 (Wickham, 2016), metR (Campitelli, 2020), ggforce (Pedersen, 2020), and ggh4x (van den Brand, 2020).

3. Results

3.1. Sub-Regions

It is important to define sub-regions of coherent interannual precipitation variability to study large-scale atmospheric drivers for the summer precipitation over STAr. Following the regionalization method presented in Section 2, four precipitation sub-regions (SR_{1-4}) for December, seven precipitation sub-regions (SR_{1-7}) for January and four precipitation sub-regions (SR_{1-4}) for February are obtained (see Fig. 3), with their corresponding PI_j time series. The large number of sub-regions for January precipitation points to a more fragmented spatial precipitation coherence, somehow expected since January is the peak month of summer convective storms (Durkee and Mote, 2010). There are some monthly precipitation sub-regions that geographically coincide: January SR_2 and SR_3 (SR_5 and SR_7) roughly match with December and February SR_2 (SR_3). The January SR_5 comprises stations in northern STAr, which are not grouped neither in December nor in February. It can be noticed that most stations from northern and western STAr are unclassified into any subregion, which highlights the localized convective nature of summer precipitation there.

3.2. Precipitation in December

All precipitation sub-regions in December show strong and significant correlation with ENSO indices suggesting a linear relationship (not shown). In Figure 4 the composite difference of SST anomalies for high minus low PI values is shown for every precipitation sub-regions. The SST composite difference fields show positive and significant anomalies over the equatorial central-eastern Pacific, resembling ENSO SST anomalies. The SST composite anomalies are accompanied by OLR (Fig. S2) and CHI (Fig. S3) composite anomalies that depict the typical ENSO characteristics such as enhanced convection over the central equatorial Pacific and the anomalous Walker cell (Cai et al., 2020), which reinforces the idea of a linear relationship with the ENSO phenomenon.

The upper level tropospheric circulation composite anomalies show an extratropical quasi-stationary Rossby wave train that propagates from east of Australia through the Pacific to southern South America for December SR_1, SR_2, and SR_3 (Fig. 5 panel a, shown only for SR_2 for simplicity). The Rossby wave imposes regional anomalous circulation that enhances (inhibits) the MF from the tropics to eastern STAr for high (low) PI values (Fig. 5 panel b). The latter implies that wet (dry) conditions over eastern STAr (SR_1, SR_2, and SR_3) are teleconnected with EN (LN) events through an extratropical quasi-stationary Rossby wave train that impose an anomalous anticyclonic (cyclonic) circulation over southeast Brazil which enhances (inhibits) northerly MF towards the region. These results are in concordance with previous works, such as Hurtado and Agosta (2021).

In contrast, the teleconnection for SR_4 differs from other subregions in the fact that it is asymmetric between high and low PI values, the reason for which the composite difference of anomalies is discouraged. Wet conditions over SR_4 (composite from high PI_j values) are associated with a subtropical quasi-stationary Rossby wave that propagates from the eastern Pacific (roughly 95° W − 30° S) to south Brazil (Fig. 6 panel a1). This is accompanied by a strengthening of the northerly MF (Fig. 6 panel b1) enhancing anomalous MF convergence in south-western STAr (SR_4). On the other hand, dry conditions over SR_4 are associated with an extratropical quasi-stationary Rossby wave that propagates from the western South Pacific to the southern coast of SA (Fig. 6 panel a2). This Rossby wave train establishes a lower tropospheric anomalous cyclonic circulation that inhibits the northerly MF to the region (Fig. 6 panel b2).

3.3. Precipitation in January

The first step to discriminate large-scale forcings on January precipitation over STAr was to assess in detail by comparison the tropospheric circulation and climatic features of every variable composite for high ($PI_j > 75^{th}$ percentile) and low ($PI_j < 25^{th}$ percentile) PI_j values for every sub-region and their differences. The assessment yielded that tropospheric circulation and climatic features are similar for SR_1, SR_2 and SR_3 (SR_4 and SR_5) in eastern (south-western) STAr and therefore can be grouped into two single sets.

3.3.1. January dry and wet conditions in eastern STAr (SR_1/SR_2/SR_3)

The regional anomalous tropospheric circulation for wet and dry conditions in eastern STAr is symmetric and their composite differences provide a complete description. Thus, dry (wet) conditions in eastern STAr are characterized by negative (positive) GH anomalies over southeastern Brazil and positive (negative) GH anomalies over Argentina (see Fig. 7 panel a). This low-level tropospheric circulation inhibits (enhances) MF from the tropics to the subtropics (see Fig. 7 panel a) generating anomalous MF divergence (convergence) over eastern STAr for low (high) PI values (not shown). In consequence, the regional anomalous tropospheric circulation imposes a convection dipole between eastern STAr and SACZ region (see Fig. 7 panel b).

The associated large-scale anomalous tropospheric circulation shows an extratropical Rossby wave train that propagates from the western South Pacific (ca. 150 − 80° W and 35° S) to SA (see Fig. 8 panel d). In the wave-source region, negative upper-tropospheric CHI anomalies are observed (see Fig. 8 panel a) accompanied with negative OLR anomalies (see Fig. 8 panel b), suggesting that the source of the Rossby wave could be an anomalous divergence in the upper tropical and subtropical troposphere. Another potential source of the Rossby wave could be an anomalous significant meridional zonal wind gradient in the subtropics west of 180° W (see Fig. 8 panel c) by conversion of

mean flow kinetic energy into eddy kinetic energy, which is proportional to the zonal wind meridional gradient (Tanaka et al., 2016).

3.3.2. January dry and wet conditions in south-western STAr (SR_4/SR_5)

January wet (dry) conditions in south-western STAr are associated with an anticyclonic (cyclonic) lower tropospheric circulation over Patagonia and the Argentinian Sea (Fig. 9 panel a). The lower level tropospheric anticyclonic circulation propitiates MF from the Atlantic Ocean to south-western STAr (Fig. 9 panel a) enhancing convection in the region (Fig. 9 panel b) during wet conditions in January. Note that a similar low-level circulation configuration is related to wet summers (Oct-Mar) in Central-West Argentina (south-western STAr) at interannual scale (Agosta, 2014). In contrast, the cyclonic circulation enhances westerly MF over south STAr (Fig. 9 panel a) inhibiting the MF convergence and convection in the region (Fig. 9 panel b).

Despite the tropospheric circulation anomalies associated with dry (wet) conditions in the region are regionally prominent, they are apparently unlinked to large-scale phenomena (not shown). Nonetheless, an extratropical quasi-stationary Rossby wave train is observed to be propagating over the South Pacific from eastern Australia to SA (Fig. 10 panel a), for some dry years in south-western STAr -5(4) out 10 years in SR_4 (SR_5). This Rossby wave seems to be generated due to anomalous divergence in the upper tropical troposphere (Fig. 10 panel b).

3.3.3. January dry and wet conditions in northern STAr (SR_6)

January wet (dry) conditions in northern STAr are associated with southward (northward) MF anomalies over north STAr, Bolivia, and Paraguay (Fig. 11 panel a). These MF anomalies enhance (inhibit) convection in north STAr (Fig. 11 panel b). The monthly low-level tropospheric circulation anomalies are weak and not significant (Fig. 11 panel a). The latter is indicative that anomalous MF, modulating precipitation anomalies in northern STAr during this year, is due to a combination of different atmospheric processes.

A visual inspection of every atmospheric field with either dry or wet conditions in northern STAr, allowed us to identify a set of 4 dry years with common tropospheric circulation features. The northward MF anomalies that propitiate the dry conditions in this set are imposed by positive (negative) GH anomalies over Argentina (southeast Brazil; Fig. 12 panel a). Such a low-level tropospheric circulation configuration is associated with an extratropical Rossby wave train that zonally propagates from the midlatitudes of western South Pacific towards SA (Fig. 12 panel c). This Rossby wave appears to be generated due to the conversion of mean flow kinetic energy into eddy kinetic energy (Fig. 12 panel b), like in the case of eastern STAr (Section 3.3.1).

3.3.4. January dry and wet conditions in central STAr (SR_7)

In Central STAr, neither dry nor wet conditions in January show common regional tropospheric circulation features (not shown). The subregion lies in the borders of the other analyzed subregions, showing thus sometimes wet and dry conditions of one sub-region in some years and sometimes wet and dry conditions of another sub-region in other years (Table 1).

Table 1: Amount of common wet/dry year between SR_7 (central STAr) and the other sub-regions.

Sub-Region	Common wet year	Common dry year
SR_1	4	3
SR_2	5	4
SR_3	3	4
SR_4	4	4
SR_5	3	4
SR_6	4	5

3.4. Precipitation in February

3.4.1. February dry and wet conditions in eastern STAr (SR_4/SR_5)

As for January, large-scale forcings of February precipitation were assessed by compositing atmospheric and SST fields for high and low PI_j values. This resulted in the fact that similar tropospheric anomaly patterns depict February precipitation in SR_1 and SR_2 (several years of their composites are in common), therefore, they are further analyzed as one subregion. On a regional scale, tropospheric circulation anomalies are symmetric between high and low PI_j values, therefore, their composite difference is further examined. Wet (dry) conditions in eastern STAr are characterized by positive (negative) GH anomalies over southeastern Brazil and negative (positive) GH anomalies over Argentina (see Fig. 13 panel a). This low-level circulation enhances (inhibits) MF from the tropics to the subtropics (see Fig. 13 panel a) generating MF divergence (convergence) over eastern STAr for low (high) PI values (not shown). In consequence, the regional anomalous air flow circulation imposes a convection dipole between the eastern STAr and SACZ regions (see Fig. 13 panel b).

For the dry conditions over eastern STAr in February, the large-scale anomalous tropospheric circulation shows an extratropical Rossby wave train that propagates from the western South Pacific (ca. 150 − 80° W and 35° S) to SA (see Fig. 14 panel b). Un-significant weak OLR and CHI anomalies are observed in the wave-source region (not shown) though zonal wind anomalies are prominent depicting a meridional gradient in the wave-source regions (see Fig. 14 panel a). In the absence of regional OLR and CHI anomalies, the conversion of mean flow kinetic energy into eddy kinetic energy seems to be again (as for SR_1, SR_2, SR_3 and SR_6 in January) the wave source (Tanaka et al., 2016).

For the wet conditions over eastern STAr in February, an anomalous Walker cell is observed as the main large-scale feature. This is evidenced by the 250hPa CHI anomaly field that shows a zonal asymmetry across the tropics, with negative anomalies over the Pacific and positive anomalies over eastern Brazil and the South Atlantic (see Fig. S4). The tropical asymmetric Walker-related anomalies are manifested also in the 500hPa omega anomalous composite field that shows upward anomalous motion in the central Pacific and downward anomalous motion over eastern Brazil and the tropical South Atlantic (not shown). It is known that the MJO perturbs both the Hadley cell and the Walker cell on intraseasonal scale (Schwendike et al., 2021), and so these February CHI anomalies may be

related to it. Figure 15 shows the MJO daily indices RMM1 and RMM2 for all days in February which are part of the wet conditions in eastern STAr. It can be seen that there is a predominance of phase 7 (35% of days), followed by phase 6 (19% of days, see Fig. 13). Thus, over 50% of the days in February with wet conditions (high PI values) are accounted for in two phases out of eight phases of the MJO combined index. These two phases are related to enhanced convection in the western equatorial Pacific (Grimm, 2019), as observed in the CHI anomalous field (see Fig. S4).

3.4.2. February dry and wet conditions in central-south STAr (SR_3)

A first visual inspection of tropospheric circulation composites for high and low PI_3 values yielded un-significant and weak anomalies suggesting mixed signals of potential physical mechanisms. A further discrimination into LN, EN and ENSO neutral (NN) events resulted in physically discernible signals for only the NN event-based composites. Thus, in NN events, the leading forcing mechanism of wet (dry) conditions in central-south STAr appears to be related to an extratropical quasi-stationary Rossby wave propagating from the subtropics of eastern Indian Ocean towards SA (see Fig. 16 panel a). The source of such a quasi-stationary Rossby wave could be linked to large-scale divergent wind anomalies observed over tropical SA and northern Africa, and global convergent wind anomalies observed over southern Asia, tropical eastern Africa and the tropical Indian Ocean (not shown). Over the southern cone of SA, the low-level flow anomalies imprint northerly (southerly) MF anomalies (see Fig. 16 panel b) and moisture divergence (convergence) anomalies over central-south STAr (see Fig. 16 panel c) leading to consistent OLR anomalies for wet (dry) conditions in the sub-region (see Fig. 16 panel d).

3.4.3. February dry and wet conditions in south-western STAr (SR_4)

As for south-western STAr wet and dry conditions in January, Wet (Dry) conditions in south-western STAr in February are associated with an anticyclonic (cyclonic) lower tropospheric circulation over Patagonia and the Argentinian Sea (see Fig. 17 panel a). This tropospheric flow favors increased (decreased) convection in south-western STAr and northern Patagonia as shown in Fig. 17 panel b. For wet conditions, negative OLR anomalies in the region are linked to moisture transport from the mid-latitude South Atlantic, while for dry conditions, positive OLR anomalies are linked to the absence of moisture transport towards the region (see Fig. 17 panel a).

Although the tropospheric circulation anomalies are regionally prominent in February, they seem not to be linked to large-scale phenomena. Hemispherical tropospheric circulation conditions in the previous month shed more light to explain the observed wet conditions in February. In Figure 18 (panel b), an extratropical quasi-stationary Rossby wave train is observed to propagate from the east of Australia (ca. 180° W and 30° S) to SA throughout January. In the wave-source region, negative upper-tropospheric CHI anomalies are observed (see Fig. 18 panel a) suggesting that the upper tropospheric tropical-subtropical anomalous divergence is the main wave source. Note that the monthly quasi-stationary Rossby wave appears to be linked to a sub-monthly Rossby wave that slowly propagates towards SA from mid-January to early February. The wet condition composites for the 15-day mean fields of upper-level low-frequency (10 > days) GH tendency anomalies from mid-January to mid-February in the period windows 17-31 Jan, 24 Jan-7 Feb and 1-15 Feb are displayed in Figure 18 (panels c-e). The panels show a slow eastward anomaly progression of positive GH tendency towards southern SA, linked to the low-frequency transient activity of the monthly quasi-stationary Rossby wave. Consequently, through convergence of vorticity fluxes over Patagonia and

surrounding areas in late January and early February, positive GH anomalies are built up in the region, which prevail throughout February (Fig. 18 panel a).

4. Conclusions

This research work focuses on climatic forcing of the summer (Dec-Feb) precipitation variability over STAr in the period 1979-2018. First, sub-regions of coherent interannual precipitation variability were determined for every month to design subregional precipitation indices, obtaining four sub-regions for December (SR_{1-4}), seven for January (SR_{1-7}) and four for February (SR_{1-4}). Then, climatic composite fields for high (wet conditions) and low (dry conditions) precipitation index values were analyzed to determine subregional precipitation forcings for every month.

Most subregional precipitation anomalies are associated with a convection dipole between eastern STAr and SACZ region, linked to the leading mode of precipitation variability in SA, and widely described in the literature. The convection dipole means enhanced (inhibited) convection in eastern STAr and inhibited (enhanced) convection in SACZ region. The associated anomalous low-level tropospheric circulation is depicted by an anticyclonic (cyclonic) flow in southeastern Brazil that enhances (inhibits) MF from the tropic to the subtropics.

At interannual time scales, the convection dipole is associated with the ENSO phenomenon (Tedeschi et al., 2013), and SST variations in the western-subtropical South Atlantic (Doyle and Barros, 2002). However, in this research work, the evidence shows that ENSO is the main forcing of precipitation in December at an interannual scale. However, its modulation is absent in January and February probably owing to non-linear relationships (Hurtado, 2022). The influence of the western-subtropical South Atlantic SST was not observed.

Wet conditions in subregions of eastern STAr are related to anomalous low-level anticyclonic tropospheric circulation in southeastern Brazil that is imposed by two different large-scale mechanisms. One mechanism is a teleconnection via a Rossby wave train propagating over the South Pacific, that is linked to EN events in December, to enhanced convection in the western tropical Pacific in January, and to conversion of mean flow kinetic energy in January and February. The other forcing mechanism is only observed in February, which is related to an anomalous Walker cell caused mainly by an active convection core in the western Pacific basin, which could probably be owing to the inter-annual variability of the frequency of MJO phases 6 and 7. Note that these MJO phases are climatically the most frequent MJO phases during austral summer (Lafleur et al., 2015).

In turn, dry conditions in subregions of eastern STAr are related to the low-level tropospheric cyclonic anomalous circulation over southeastern Brazil, associated with a Rossby wave train that propagates over the South Pacific. The nature of the Rossby wave source is linked to LN-event upper level divergence anomalies in December, and to conversion of the mean flow kinetic energy in January and February.

In addition, wet (dry) conditions in subregions of southwestern STAr in January and February are associated with a mid-latitude anomalous anticyclonic (cyclonic) low-level tropospheric circulation over Patagonia and the Argentinian Sea that enhances (inhibits) moisture convergence in southwestern STAr. For dry conditions in January, the latter mid-latitude tropospheric cyclonic anomaly is partially forced by a Rossby wave train that propagates from east Australia to SA through the South Pacific. For wet conditions in February, the latter mid-latitude tropospheric anticyclonic

circulation anomaly appears to be generated by vorticity flux convergence associated with a sub-monthly quasi-stationary Rossby wave that is active from the previous month (January), which generates positive GH anomalies over Patagonia and surrounding areas. Further understanding of the latter mechanism could contribute to forecast monthly precipitation anomalies in the region, which is left for future research.

acknowledgements

The current research was funded by the PPID-G008 from the National University of La Plata title: "Extremos húmedos y secos en Argentina. Análisis de los cambios proyectados para fines del siglo XXI". The current research was funded, aslo, by the PIP 1220200102257CO from CONICET title: "Cambios observados en la intensidad, frecuencia y duración de eventos extremos de precipitación y sus proyecciones futuras con modelos HigResMIP (CMIP6) en la región nordeste de Argentina ". We wish to express our gratitude to the Carmelite NGO for the financial support.

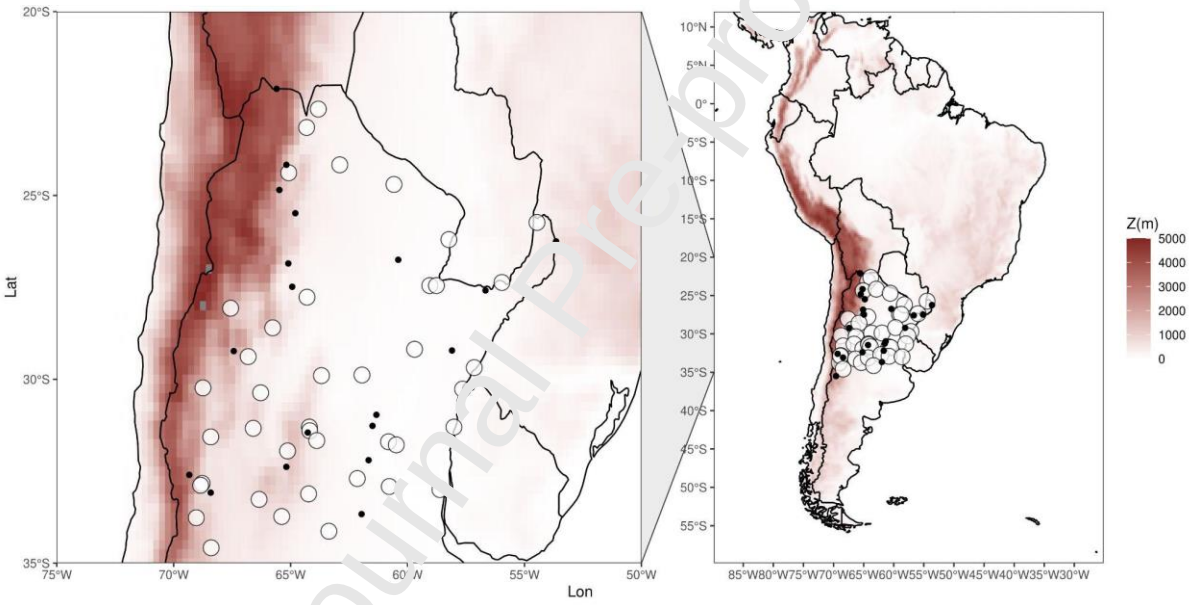

Figure 1: Location of the 62 weather stations in Subtropical Argentina. Larger white dots indicate the stations used for regionalization (see Section 2). In red shaded scale is shown the ERA5 topography.

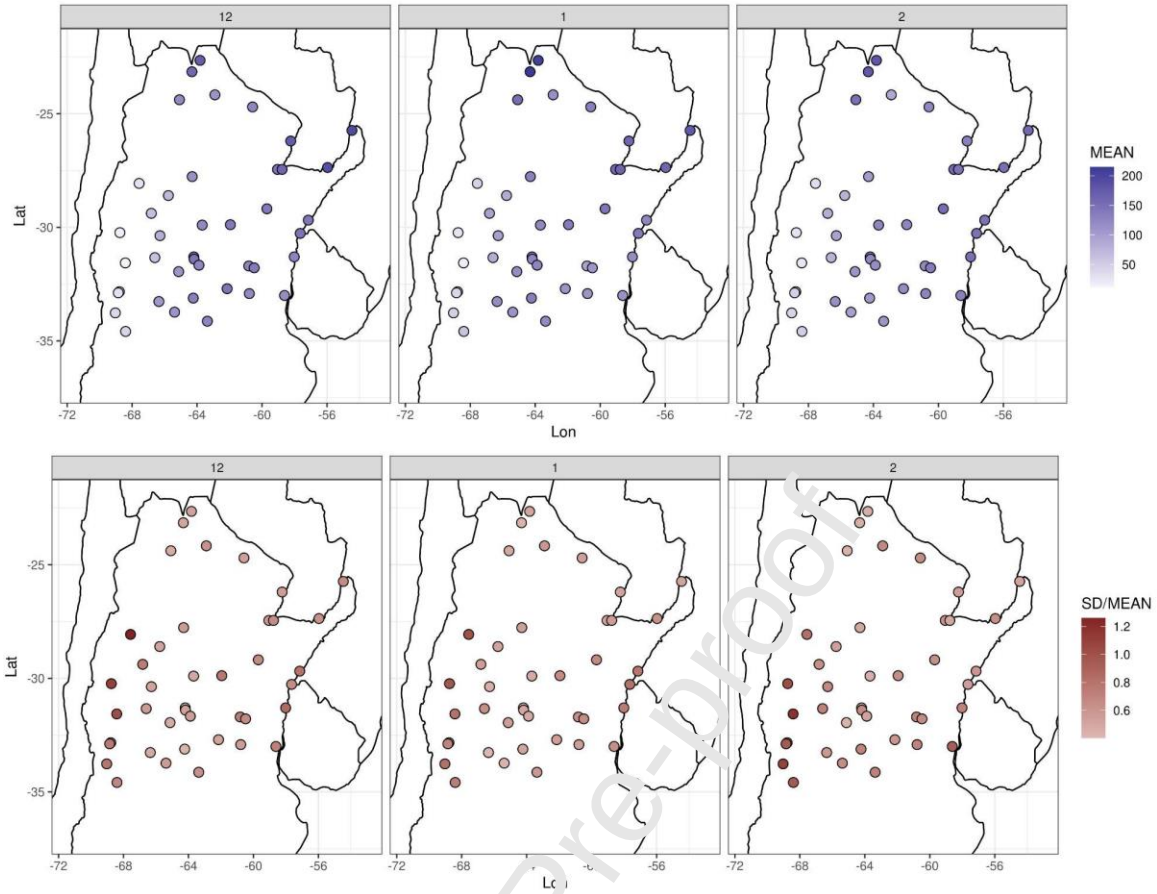

Figure 2: Upper panels: Monthly mean precipitation for each weather station in December (left panel), January (middle panel) and February (right panel). Lower panels: As the upper panels but for the precipitation coefficient of variation which is the ratio of the standard deviation to the mean.

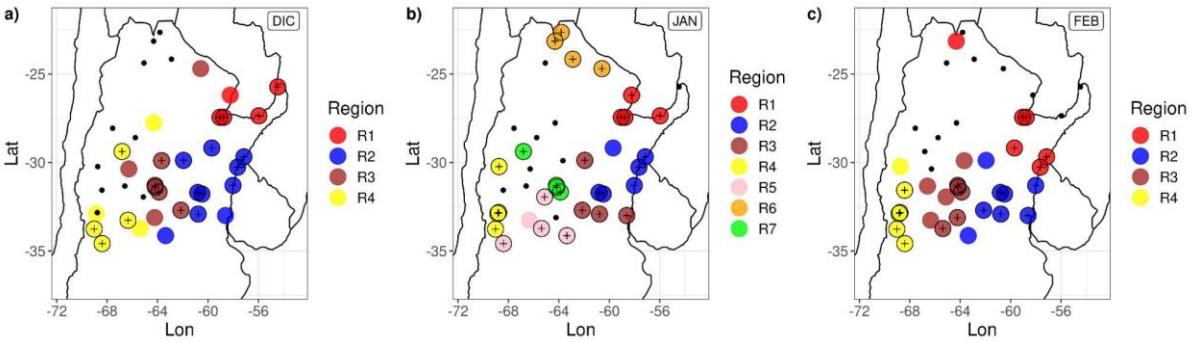

Figure 3: Subregions of coherent precipitation co-variability in STAr for December (panel a), January (panel b) and February (panel c).Each color represent a different subregion. Closed dots with a "plus" mark indicate the location of stations used to design the PI. Black dots are locations of stations that were not grouped by the methodology.

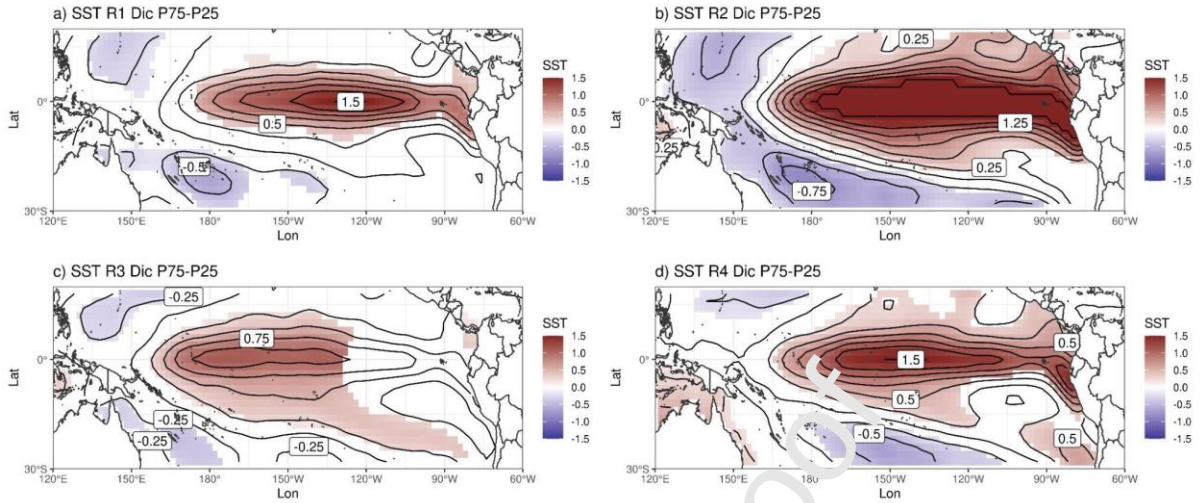

Figure 4: December composite difference anomalies of SST for high PI values (PI > P^{th} 75) minus low PI values (PI < P^{th} 25) in SR_1 (panel a), SR_2 (panel b), SR_3 (panel c) and SR_4 (panel d). Color shades, 90% confidence level.

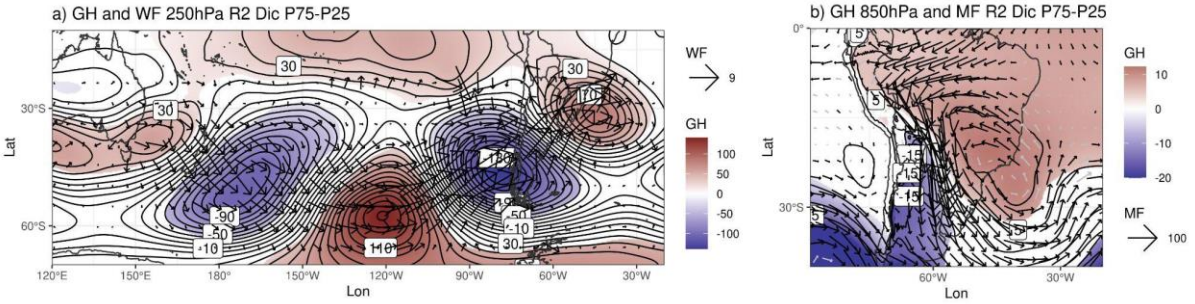

Figure 5: Panel a: December composite difference anomalies of GH and WF at 250hPa for high PI values (PI > P^{th} 75) minus low PI values (PI < P^{th} 25) in SR_2. Panel b: December composite difference anomalies of GH at 850hPa and MF for high PI values (PI > P^{th} 75) minus low PI values (PI < P^{th} 25) in SR_2. Color shades, 90% confidence level. Black arrows in panel b stand for significant MF anomalies at 90% confidence level.

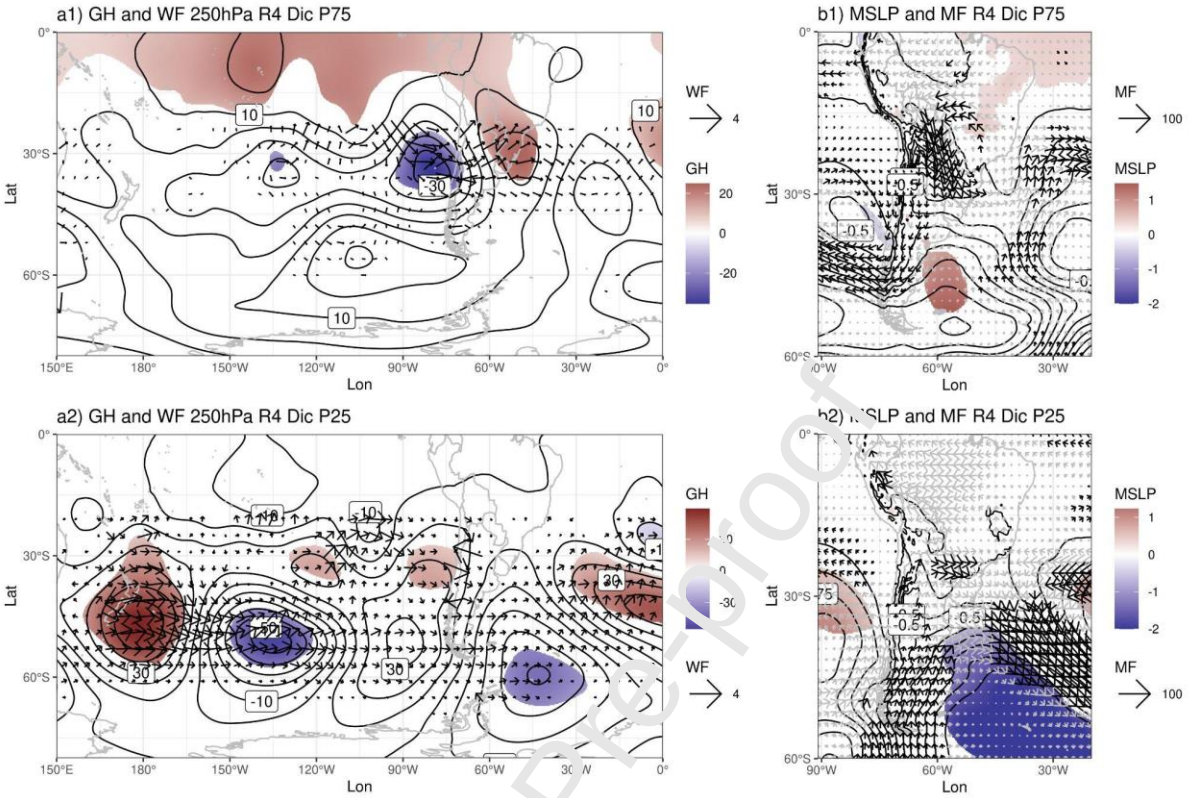

Figure 6: Panels a: December composite anomalies of GH and WF (in m 2 /s 2) at 250hPa for high PI values (PI > P^{th} 75, panel a1) and low PI values (PI < P^{th} 25, panel a1) in SR_4. Panels b: December composite anomalies of MSLP and MF (in $kg * m^{-1} s^{-1}$) for high PI values (PI > P^{th} 75, panel b1) and low PI values (PI < P^{th} 25, panel b2) in SR_4. Color shades, 90% confidence level. Black arrows in panels b stand for significant MF anomalies at 90% confidence level. Anomalies baseline period 1980-2010.

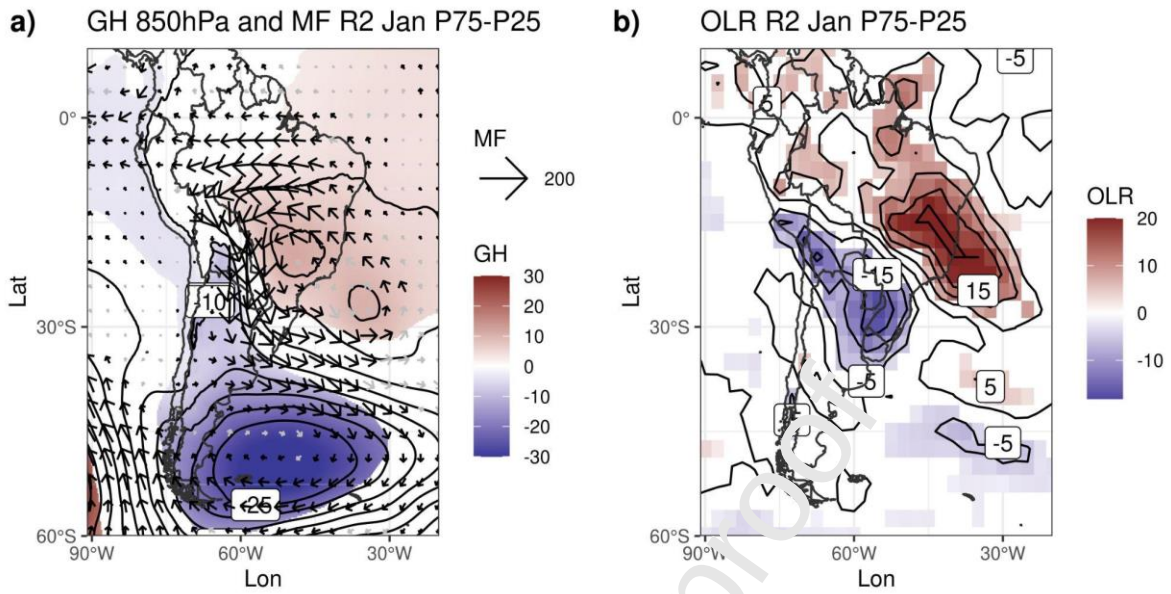

Figure 7: January composite difference anomalies of GH at 850hPa and MF (panel a) and OLR (panel b) for high PI values (PI > P^{th} 75) minus low PI values (PI < P^{th} 25) in SR_2. Color shades, 90% confidence level. Black arrows in panel a stand for significant MF anomalies at 90% confidence level.

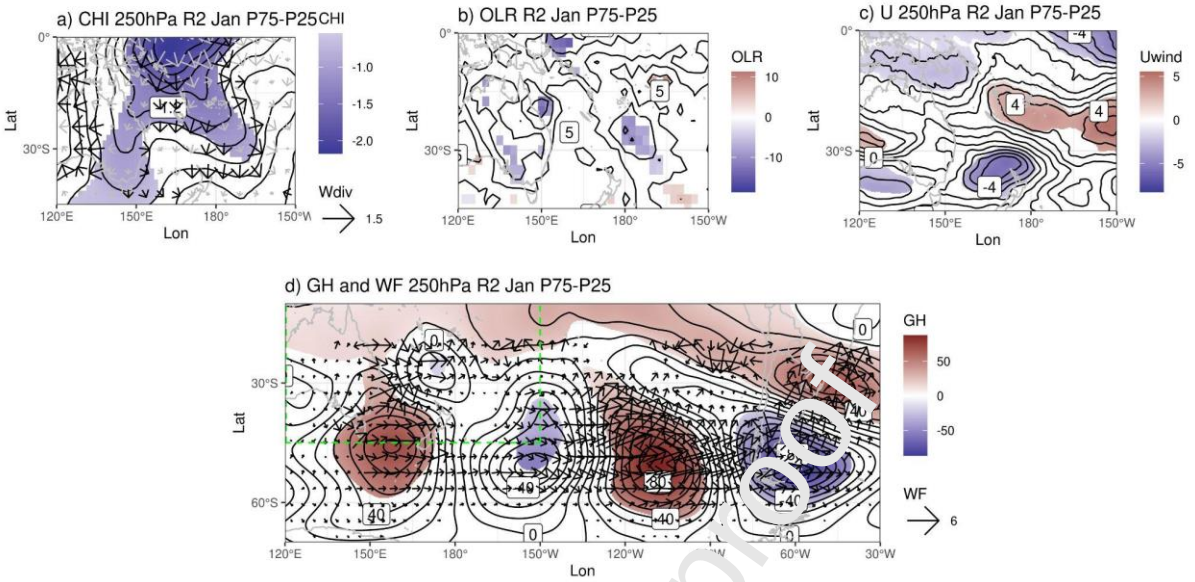

Figure 8: January composite difference anomalies of CHI and divergent wind (panel a), OLR (panel b), zonal wind at 250hPa (panel c) and GH and WF at 250hPa (panel d) for high PI values (PI > P^{th} 75) minus low PI values (PI < P^{th} 25) in SR_2. Color shades, 90% confidence level. Black arrows in panel a stand for significant divergent wind anomalies at 90% confidence level. The green stroked-line inset in panel d denotes the map area of panels a-c.

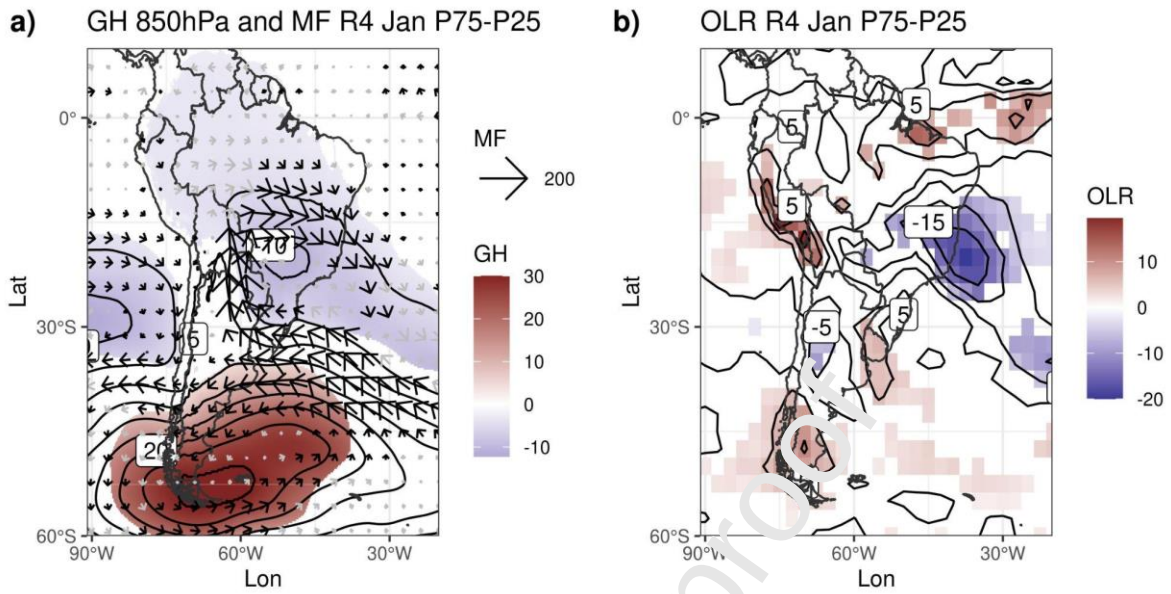

Figure 9: January composite difference anomalies of GH at 850hPa and MF (panel a) and OLR (panel b) for high PI values (PI > P^{th} 75) minus low PI values (PI < P^{th} 25) in SR_4. Color shades, 90% confidence level. Black arrows in panel a stand for significant MF anomalies at 90% confidence level.

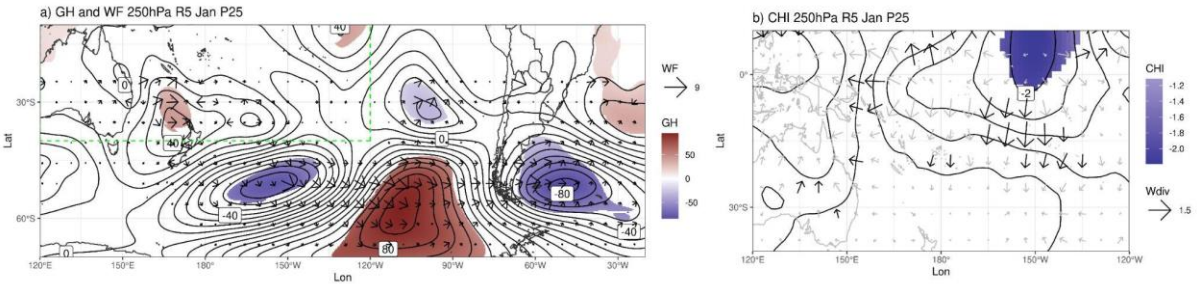

Figure 10: January composite anomalies of GH and WF at 250hPa (panel a) and CHI and divergent wind (panel b) for low PI values (PI < P^{th} 25) in SR_4. Color shades, 90% confidence level. Black arrows in panel b stand for significant divergent wind anomalies at 90% confidence level. The green stroked-line inset in panel a denotes the map area of panels b. Anomalies baseline period 1980-2010.

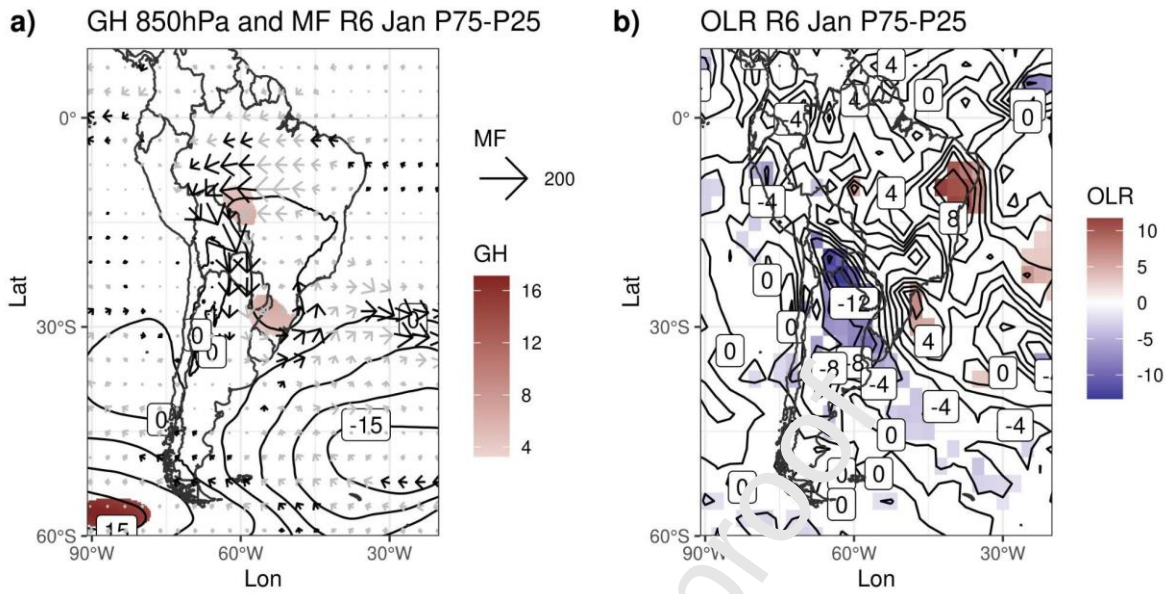

Figure 11: January composite difference anomalies of GH at 850hPa and MF (panel a) and OLR (panel b) for high PI values (PI > P^{th} 75) minus low PI values (PI < P^{th} 25) in SR_6. Color shades, 90% confidence level. Black arrows in panel a stand for significant MF anomalies at 90% confidence level.

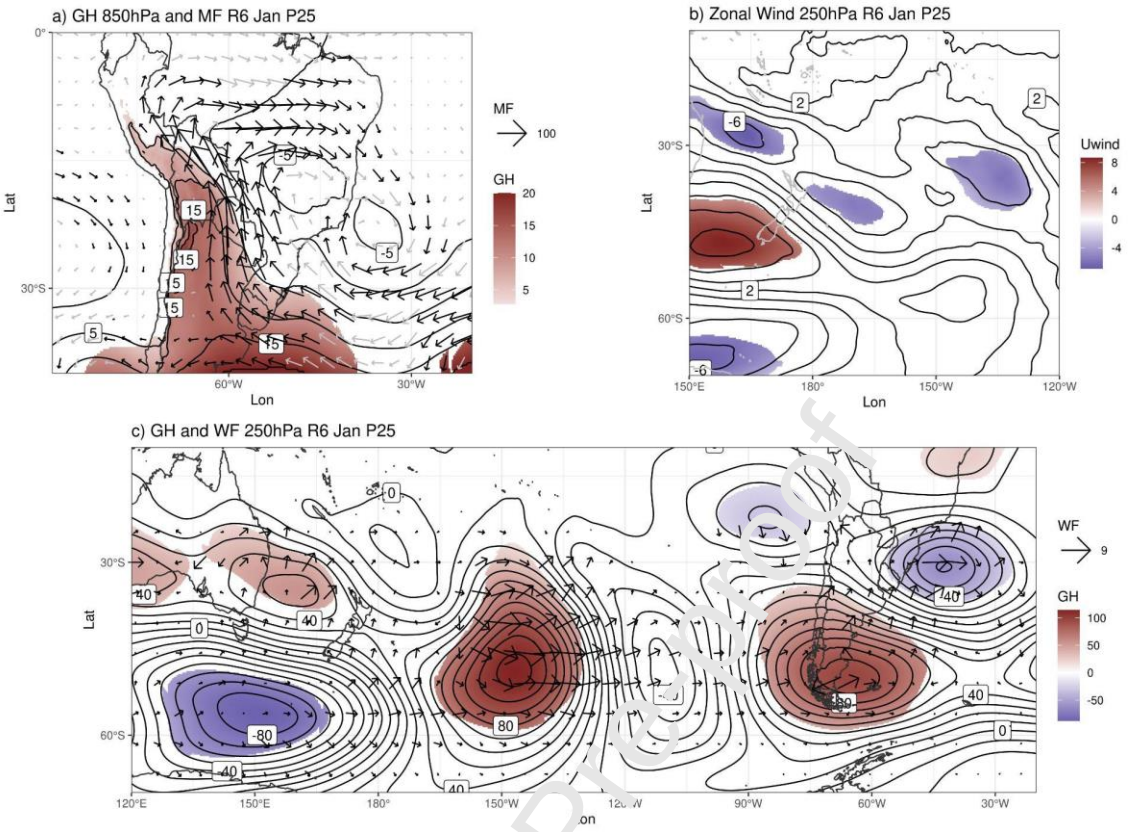

Figure 12: January composite anomalies of GH at 850hPa and MF (panel a), zonal wind at 250hPa (b), GH and WF at 250hPa (panel c) for low PI values (PI < P^{th} 25) in SR_6. Color shades, 90% confidence level. Black arrows in panel a) stand for significant MF anomalies at 90% confidence level. Anomalies baseline period 1980-2010.

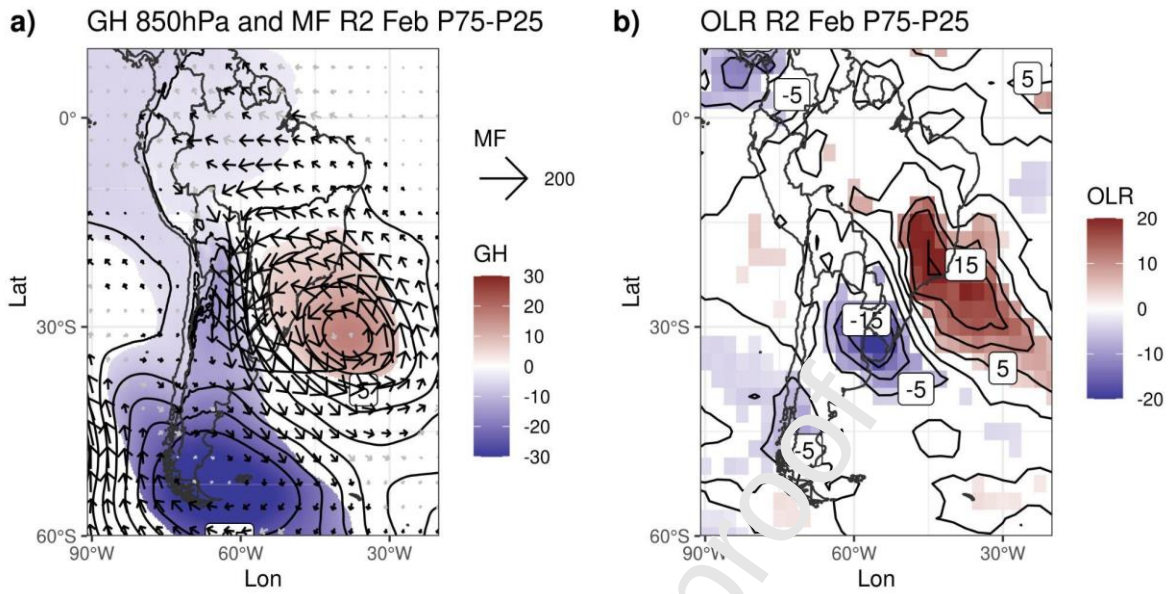

Figure 13: February composite difference anomalies of GH at 850hPa and MF (panel a) and OLR (panel b) for high PI values (PI > P^{th}75) minus low PI values (PI < P^{th} 25) in SR_2. Color shades, 90% confidence level. Black arrows in panel a stand for significant MF anomalies at 90% confidence level.

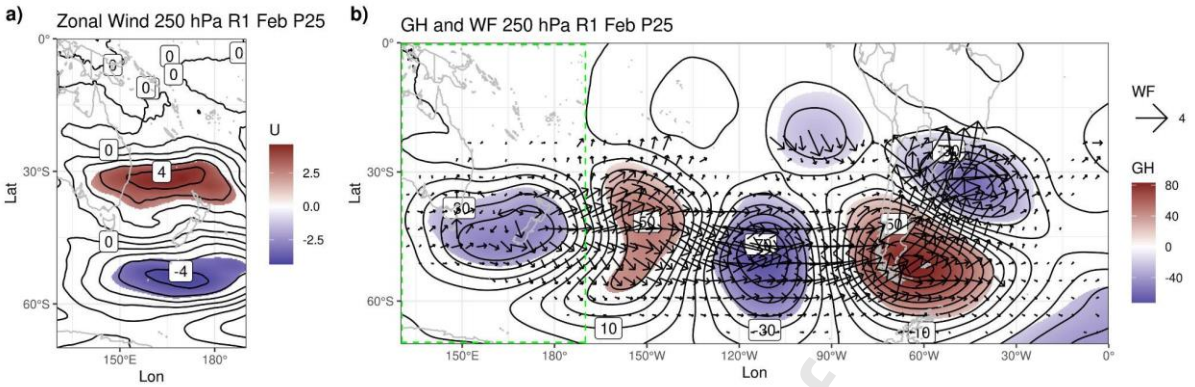

Figure 14: February composite anomalies of zonal wind at 250hPa (a) and GH and WF at 250hPa (panel b) for low PI values (PI < $P^{th}25$) in SR_1. Color shades, 90% confidence level. Black arrows in panel b stand for significant divergent wind anomalies at 90% confidence level. The green stroked-line inset in panel b denotes the map area of panels a. Anomalies baseline period 1980-2010.

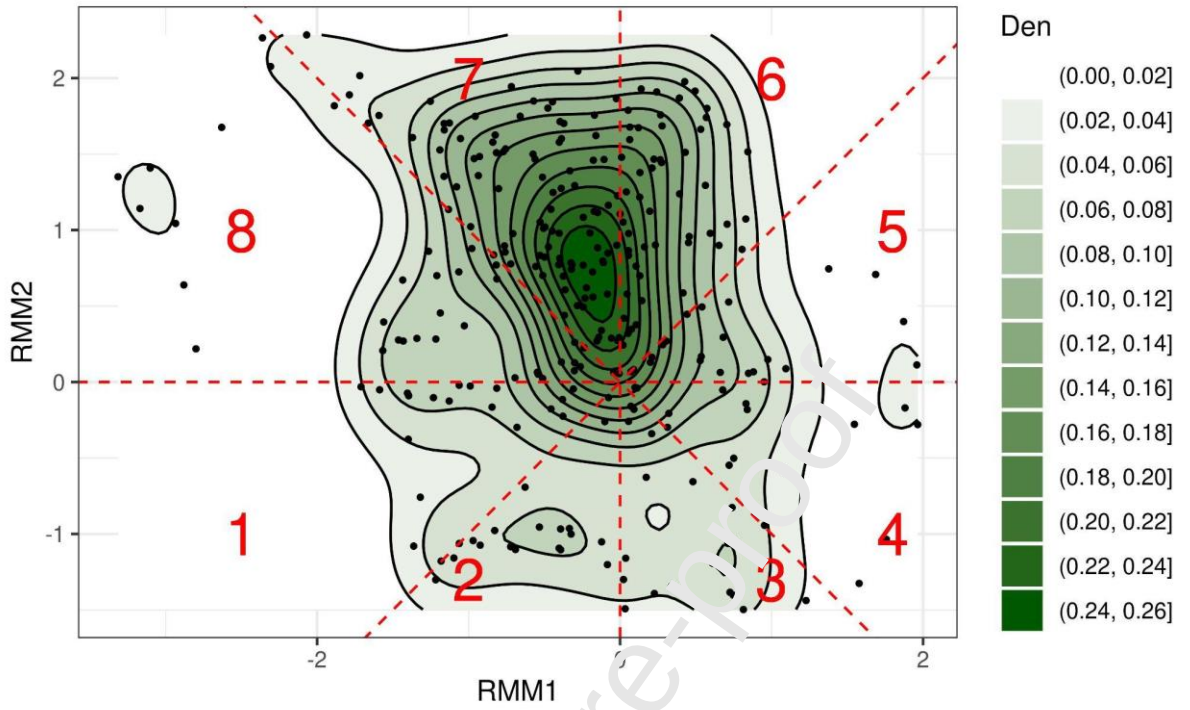

Figure 15: MJO multivariate index, RMM1 and RMM2, for all days in February with high PI values in SR_2 ($PI_2 > P^{th}$ 75) are shown in black dots. The eight phases of the MJO are indicated in red color. A two-dimensional Gaussian kernel density estimation is shown in green shades. In this sense the colour scale, Den, is the empirical estimated Probability Density Function of RMM1 and RMM2 for the days in February with high PI values in SR_2.

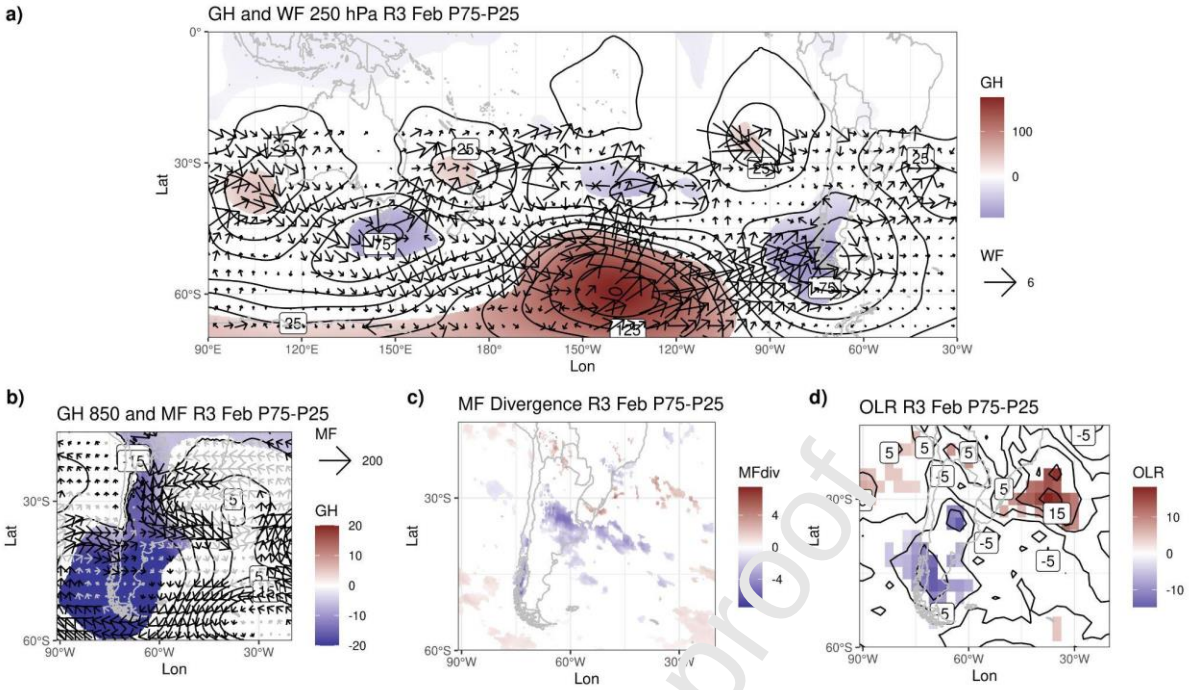

Figure 16: February composite difference anomalies GH and WF at 250hPa (panel a), 850hPa GH and MF (panel b), MF divergence (panel c), and OLR (panels d) for high PI values (PI > P^{th} 75) minus low PI values (PI < P^{th} 25) in SR_3 for NN events. Color shades stand for significant anomalies at a 90% confidence level. Black arrows in panel b stand for significant MF anomalies at 90% confidence level.

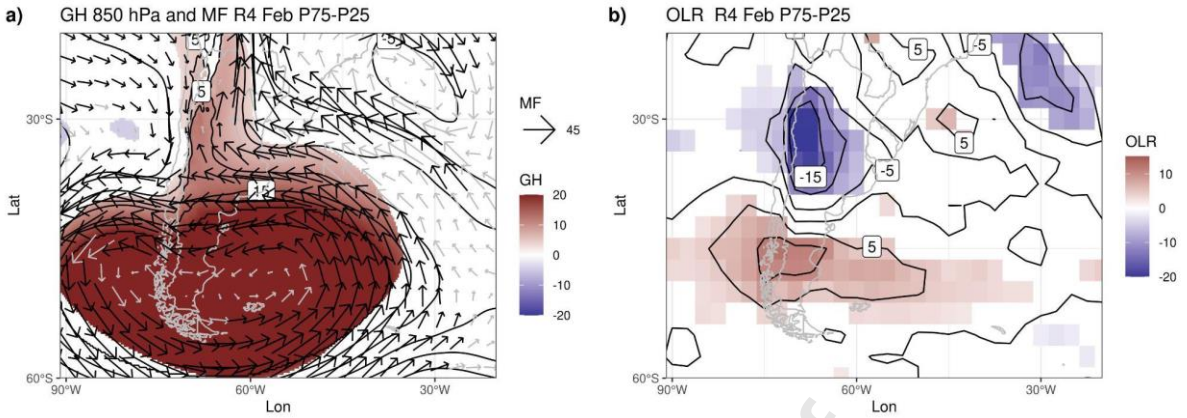

Figure 17: February composite difference anomalies of GH at 850hPa and MF (panel a) and OLR (panel b) for high PI values (PI > P^{th} 75) minus low PI values (PI < P^{th} 25) in SR_4 . Color shades, 90% confidence level. Black arrows in panel a stand for significant MF anomalies at 90% confidence level.

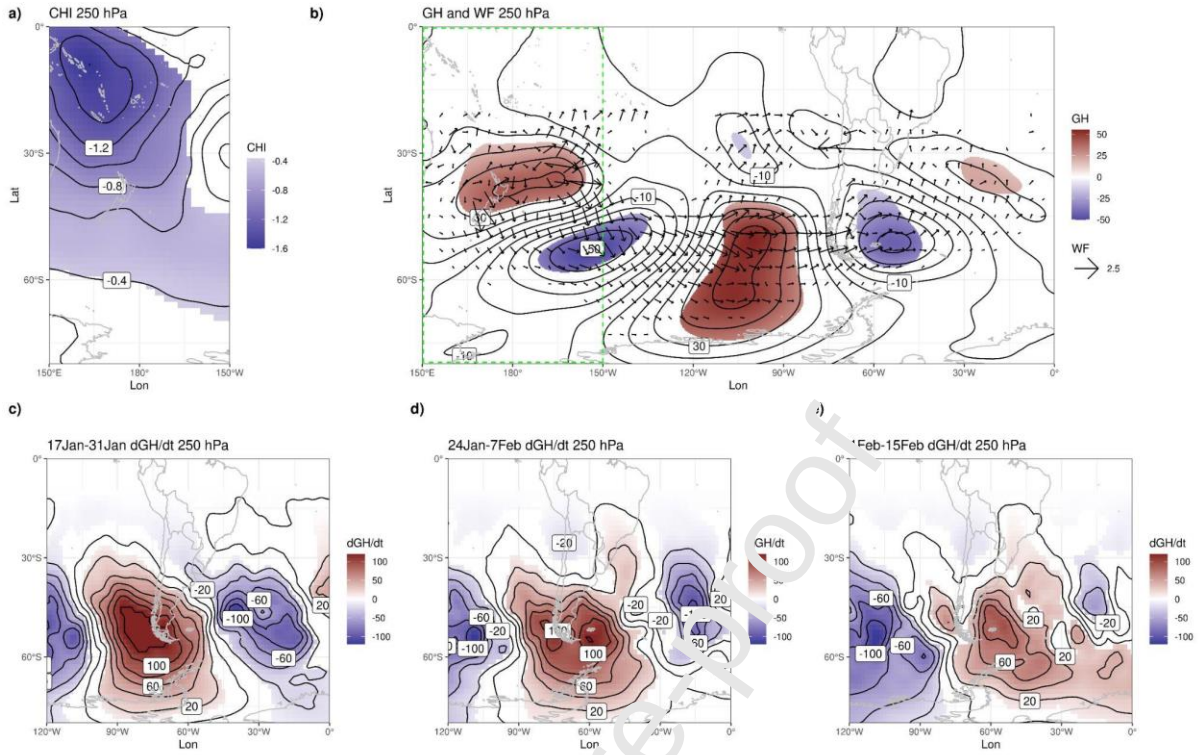

Figure 18: Upper panels: January composite anomalies of CHI at 250hPa (panel a), and GH and WF 250hPa (panel b) prior to February with high PI values in SR_4 ($PI_4 > P^{th}$ 75). The green stroked-line inset in panel b denotes the map area of panel a. Lower panels: 15-day period mean composite of the low-frequency 250hPa GH tendency anomalies for the periods January 17th - January 31th (panel c), January 24th - February 7th (panel d), and February 1st - February 15th (panel e), associated with high PI values in SR_4 ($PI_4 > P^{th}$ 75) in February. In all panels, color shades stand for significant anomalies at a 90% confidence level. Anomalies baseline period 1980-2010.

Appendices

A. Regionalization Method

The regionalization method is based on the subregional Precipitation Index (PI) define by Agosta et al. (1999), being:

$$PI_j(y) = \frac{1}{N}\sum_{s=1}^{N}\left(\frac{PP_s(y)}{MEAN(PP_s)} - 1\right)$$

For a subregion j, N is the amount of stations in it, s refers to each station of subregion j, y to years, $PP_s(y)$ is the monthly precipitation at station s and year y, and M EAN (PP_s) is the mean of $PP_s(y)$ regarding all years. In essence, the PI_j is the averaged across stations in subregion j of the standardized monthly precipitation.

The regionalization (grouping of stations) was done with a method that looks for the greatest region (maximization of N) in which the PI is representative of the interannual variability. It was considered that the PI was representative of the interannual variability from station s if the Pearson's first-moment correlation was greater than a threshold (r_c), cor(PI_j , PP_s) > r_c . In the current work the used threshold was r_c = 0.75. The regionalization procedure is summarized in the following diagram:

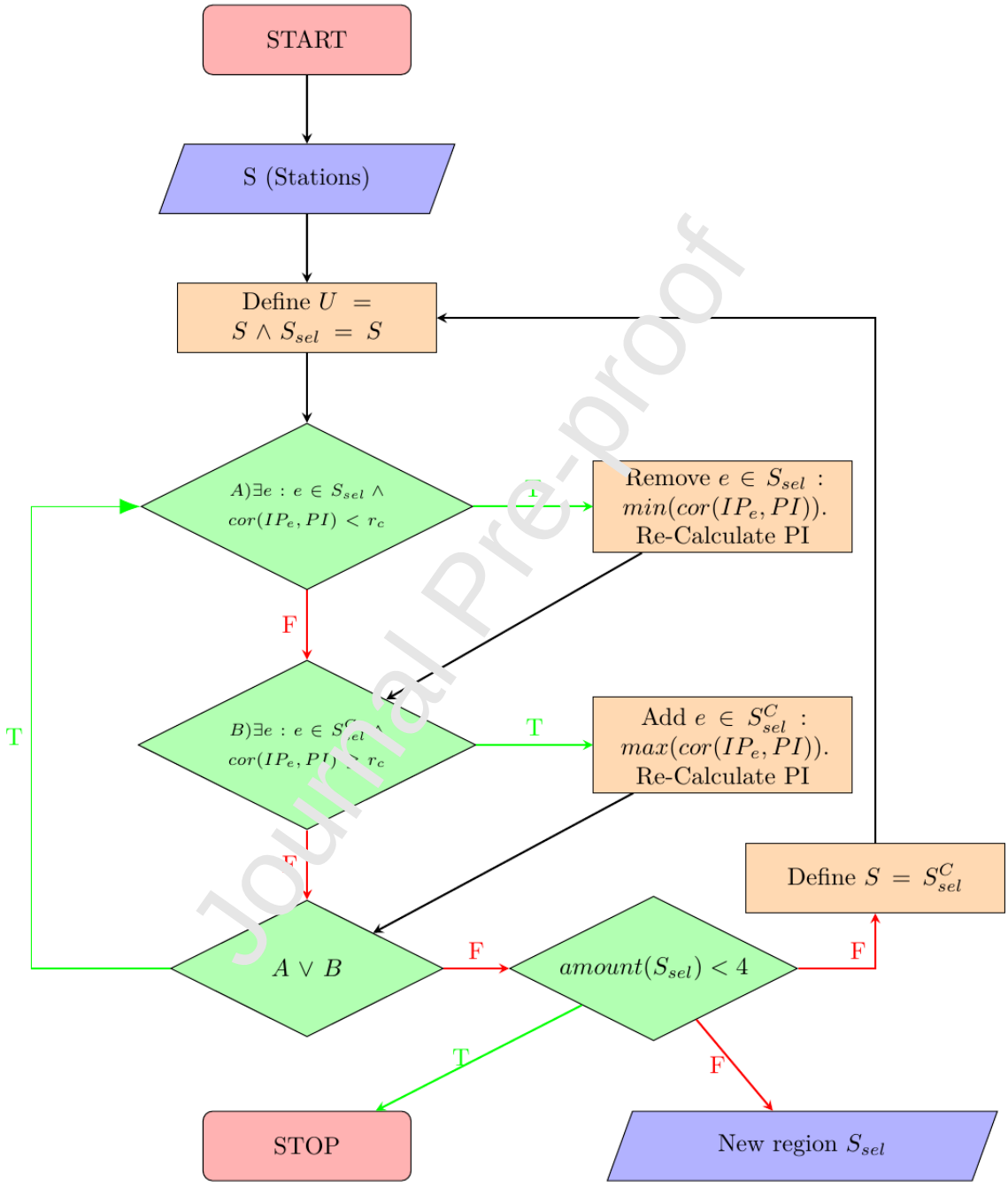

Where the pink rectangles are the beginning and end of the algorithm (terminals), the beige rectangles are process, the green diamonds are if-else statements (decisions), the violet rhomboids are input/output data, and the green (red) flow-lines indicates the flow of the algorithm if a decision is TRUE (FALSE). The S represent the set of stations, U the universe, and S_{sel} the selected stations for C making a region (being S^C_{sel} the complement of S_{sel}).

The procedure starts using all available stations to make the PI, and then it starts an iterative process where it can add and/or remove stations. There are two conditions, condition A that check if there is a station in S_{sel}l that has a correlation lower than r_c and condition B that check if there is a C station in S_{sel} that has a correlation higher-equal to r_c. In each condition, if it is fulfilled (TRUE) the C selected stations (S_{sel}) are modified by removing (adding) the station from S_{sel} (S^C_{sel}) that has the lowest (highest) correlation with the PI. This is repeated until conditions A and B are both FALSE.

Then, the selected stations (S_{sel}) are considered a region. If the region has at least four stations C the region is saved to use, and its stations are removed from the stations set (define $S = S_{sel}$). So the entire procedure is repeated with all the stations that were not used in the defined region/s. The algorithm keeps defining regions until the last defined region has less than four stations.

This methodology guarantees that the PI captures the variability of the used stations since it is imposed to have a high correlation. Furthermore, the combination of conditions A and B in an iterative process looks for the maximization of the number of stations present in each region.

References

Agosta, E., Compagnucci, R., Vargas, W., 1999. Cambios en el régimen interanual de la precipitación estival en la región centro-oeste argentina. Meteorol 24, 63–84.

Agosta, E.A., 2014. The 18.6-year nodal tidal cycle and the bi-decadal precipitation oscillation over the plains to the east of subtropical andes, south america. International Journal of Climatology 34, 1606–1614.

Agosta, E.A., Compagnucci, R.H., 2012. Central-West Argentina Summer Precipitation Variability and Atmospheric Teleconnections. Journal of Climate 25, 1657–1677. URL: http://journals.ametsoc.org/doi/abs/10.1175/JCLI-D-11-00206.1, doi:10.1175/JCLI-D-11-00206.1.

Agosta, E.A., Martin, P.B., Serio, L.A., 2019. Persistent easterly winds leading to precipitation in the atlantic coast of patagonia. International Journal of Climatology 39, 5063–5090.

Barreiro, M., 2010. Influence of enso and the south atlantic ocean on climate predictability over southeastern south america. Climate dynamics 35, 1493–1508.

Barros, V.R., Doyle, M.E., Camilloni, I.A., 2008. Precipitation trends in southeastern South America: relationship with ENSO phases and with low-level circulation. Theoretical and Applied Climatology 93, 19–33. URL: http://link.springer.com/10.1007/s00704-007-0329-x, doi:10.1007/s00704-007-0329-x.

Cai, W., McPhaden, M.J., Grimm, A.M., Rodrigues, R.R., Taschetto, A.S., Garreaud, R.D., Dewitte, B., Poveda, G., Ham, Y.G., Santoso, A., et al., 2020. Climate impacts of the el niño–southern oscillation on south america. Nature Reviews Earth & Environment 1, 215–231.

Campitelli, E., 2020. metR: Tools for Easier Analysis of Meteorological Fields. URL: https://github.com/eliocamp/metR, doi:10.5281/zenodo.2593516. r package version 0.8.0.

Carvalho, M., Melo-Gonçalves, P., Teixeira, J., Rocha, A., 2016. Regionalization of europe based on a k-means cluster analysis of the climate change of temperatures and precipitation. Physics and Chemistry of the Earth, Parts A/B/C 94, 22–28.

Cazes-Boezio, G., Robertson, A.W., Mechoso, C.R., 2003. Seasonal dependence of enso teleconnections over south america and relationships with precipitation in uruguay. Journal of Climate 16, 1159–1176.

Compagnucci, R., Agosta, E., Vargas, W., 2002. Climatic change and quasi-oscillations in central-west argentina summer precipitation: main features and coherent behaviour with southern african region. Climate Dynamics 18, 421–435.

Cuya, D.G.P., Brandimarte, L., Popescu, I., Alterach, J., Peviani, M., 2013. A gis-based assessment of maximum potential hydropower production in la plata basin under global changes. Renewable energy 50, 103–114.

Díaz, L.B., Saurral, R.I., Vera, C.S., 2021. Assessment of south america summer rainfall climatology and trends in a set of global climate models large ensembles. International Journal of Climatology 41, E59–E77.

Doyle, M.E., Barros, V.R., 2002. Midsummer low-level circulation and precipitation in subtropical south america and related sea surface temperature anomalies in the south atlantic. Journal of Climate 15, 3394–3410.

Durkee, J.D., Mote, T.L., 2010. A climatology of warm-season mesoscale convective complexes in subtropical south america. International Journal of Climatology: A Journal of the Royal Meteorological Society 30, 418–431.

González, M.H., Cariaga, M.L., Silansi, M.d.l.M., 2012. Some factors that influence seasonal precipitation in argentinean chaco. Advances in Meteorology 2012.

Grimm, A.M., 2003. The el niño impact on the summer monsoon in brazil: regional processes versus remote influences. Journal of Climate 16, 263–280.

Grimm, A.M., 2011. Interannual climate variability in south america: impacts on seasonal precipitation, extreme events, and possible effects of climate change. Stochastic Environmental Research and Risk Assessment 25, 537–554.

Grimm, A.M., 2019. Madden–julian oscillation impacts on south american summer monsoon season: precipitation anomalies, extreme events, teleconnections, and role in the mjo cycle. Climate dynamics 53, 907–932.

Grimm, A.M., Barros, V.R., Doyle, M.E., 2000. Climate variability in southern south america associated with el niño and la niña events. Journal of climate 13, 35–58.

Grimm, A.M., Zilli, M.T., 2009. Interannual variability and seasonal evolution of summer monsoon rainfall in south america. Journal of Climate 22, 2257–2275.

Guntu, R.K., Maheswaran, R., Agarwal, A., Singh, V.P., 2020. Accounting for temporal variability for improved precipitation regionalization based on self-organizing map coupled with information theory. Journal of Hydrology 590, 125236.

Hersbach, H., Bell, B., Berrisford, P., Biavati, G., Horányi, A., Muñoz Sabater, J., Nicolas, J., Peubey, C., Radu, R., Rozum, I., et al., 2018. Era5 hourly data on pressure levels from 1979 to present. Copernicus Climate Change Service (C3S) Climate Data Store (CDS). Available online: https://cds.climate. copernicus. eu/cdsapp .

Hersbach, H., Bell, B., Berrisford, P., Biavati, G., Horányi, A., Muñoz Sabater, J., Nicolas, J., Peubey, C., Radu, R., Rozum, I., et al., 2019a. Era5 monthly averaged data on pressure levels from 1979 to present. Copernicus Climate Change Service (C3S) Climate Data Store (CDS) 10.

Hersbach, H., Bell, B., Berrisford, P., Biavati, G., Horányi, A., Muñoz Sabater, J., Nicolas, J., Peubey, C., Radu, R., Rozum, I., et al., 2019b. Era5 monthly averaged data on single levels from 1979 to present. Copernicus Climate Change Service (C3S) Climate Data Store (CDS) 10.

Hersbach, H., Bell, B., Berrisford, P., Hirahara, S., Horányi, A., Muñoz-Sabater, J., Nicolas, J., Peubey, C., Radu, R., Schepers, D., et al., 2020. The era5 global reanalysis. Quarterly Journal of the Royal Meteorological Society .

Hurtado, S.I., 2022. Precipitación observada en la temporada húmeda sobre Argentina subtropical: calidad de datos, variabilidad y forzantes asociados de gran escala. Ph.D. thesis. Universidad Nacional de La Plata.

Hurtado, S.I., Agosta, E.A., 2021. El niño southern oscillation-related precipitation anomaly variability over eastern subtropical south america: Atypical precipitation seasons. International Journal of Climatology .

Hurtado, S.I., Zaninelli, P.G., Agosta, E.A., 2020. A multi-breakpoint methodology to detect changes in climatic time series. an application to wet season precipitation in subtropical argentina. Atmospheric Research , 104955.

Hurtado, S.I., Zaninelli, P.G., Agosta, E.A., Ricetti, L., 2021. Infilling methods for monthly precipitation records with poor station network density in subtropical argentina. Atmospheric Research , 105482.

Junquas, C., Vera, C., Li, L., Le Treut, H., 2012. Summer precipitation variability over southeastern south america in a global warming scenario. Climate dynamics 38, 1867–1883.

Lafleur, D.M., Barrett, B.S., Henderson, G.R., 2015. Some climatological aspects of the madden–julian oscillation (mjo). Journal of Climate 28, 6039–6053.

Lau, N.C., Holopainen, E.O., 1984. Transient eddy forcing of the time-mean flow as identified by geopotential tendencies. Journal of Atmospheric Sciences 41, 313–328.

Lavin-Gullon, A., Feijoo, M., Solman, S., Fernandez, J., da Rocha, R., Bettolli, M., 2021. Synoptic forcing associated with extreme precipitation events over southeastern south america as depicted by a cordex fps set of convection-permitting rcms. Climate Dynamics 56, 3187–3203.

Liebmann, B., Smith, C.A., 1996. Description of a complete (interpolated) outgoing longwave radiation dataset. Bulletin of the American Meteorological Society 77, 1275–1277.

Ma, H.Y., Ji, X., Neelin, J., Mechoso, C., 2011. Mechanisms for precipitation variability of the eastern brazil/sacz convective margin. Journal of climate 24, 3445–3456.

Magrin, G.O., Travasso, M.I., Rodríguez, G.R., 2005. Changes in climate and crop production during the 20th century in argentina. Climatic change 72, 229–249.

Marengo, J., Liebmann, B., Grimm, A., Misra, V., Silva Dias, P., Cavalcanti, I., Carvalho, L., Berbery, E., Ambrizzi, T., Vera, C.S., et al., 2012. Recent developments on the south american monsoon system. International Journal of Climatology 32, 1–21.

Mills, G.F., 1995. Principal component analysis of precipitation and rainfall regionalization in spain. Theoretical and Applied Climatology 50, 169–183.

Montini, T.L., Jones, C., Carvalho, L.M., 2019. The south american low-level jet: a new climatology, variability, and changes. Journal of Geophysical Research: Atmospheres 124, 1200–1218.

Moser, B.K., Stevens, G.R., 1992. Homogeneity of variance in the two-sample means test. The American Statistician 46, 19–21.

Pedersen, T.L., 2020. ggforce: Accelerating 'ggplot2'. URL: https://CRAN.R-project.org/package=ggforce. r package version 0.3.2.

Penalba, O.C., Vargas, W.M., 2008. Variability of low monthly rainfall in la plata basin. Meteorological Applications: A journal of forecasting, practical applications, training techniques and modelling 15, 313–323. URL: https://doi.org/10.1002/met.68.

Robledo, F., Vera, C., Penalba, O., 2020. Multi-scale features of the co-variability between global sea surface temperature anomalies and daily extreme rainfall in argentina. International Journal of Climatology 40, 4289–4299.

Roushangar, K., Alizadeh, F., 2018. A multiscale spatio-temporal framework to regionalize annual precipitation using k-means and self-organizing map technique. Journal of Mountain Science 15, 1481–1497.

Rusticucci, M., Penalba, O., 2000. Interdecadal changes in the precipitation seasonal cycle over southern south america and their relationship with surface temperature. Climate Research 16, 1–15.

Schwendike, J., Berry, G.J., Fodor, K., Reeder, M.J., 2021. On the relationship between the madden-julian oscillation and the hadley and walker circulations. Journal of Geophysical Research: Atmospheres 126, e2019JD032117.

Takahashi, K., Montecinos, A., Goubanova, K., Dewitte, B., 2011. ENSO regimes: Reinterpreting the canonical and Modoki El Niño. Geophysical Research Letters 38, n/a–n/a. URL: http://doi.wiley.com/10.1029/2011GL047364, doi:10.1029/2011GL047364.

Takaya, K., Nakamura, H., 2001. A formulation of a phase-independent wave-activity flux for stationary and migratory quasigeostrophic eddies on a zonally varying basic flow. Journal of the Atmospheric Sciences 58, 608–627.

Tanaka, S., Nishii, K., Nakamura, H., 2016. Vertical structure and energetics of the western pacific teleconnection pattern. Journal of Climate 29, 6597–6616.

Tedeschi, R.G., Cavalcanti, I.F., Grimm, A.M., 2013. Influences of two types of enso on south american precipitation. International Journal of Climatology 33, 1387–1400.

Tedeschi, R.G., Grimm, A.M., Cavalcanti, I.F., 2015. Influence of central and east enso on extreme events of precipitation in south america during austral spring and summer. International Journal of Climatology 35, 2045–2064.

van den Brand, T., 2020. ggh4x: Hacks for 'ggplot2'. URL: https://github.com/teunbrand/ggh4x. rpackage version 0.1.0.9000.

Van Der Wiel, K., Matthews, A.J., Stevens, D.P., Joshi, M.M., 2015. A dynamical framework for the origin of the diagonal south pacific and south atlantic convergence zones. Quarterly Journal of the Royal Meteorological Society 141, 1997–2010.

Vera, C., Higgins, W., Amador, J., Ambrizzi, T., Garreaud, R., Gochis, D., Gutzler, D., Lettenmaier, D., Marengo, J., Mechoso, C., et al., 2006. Toward a unified view of the american monsoon systems. Journal of climate 19, 4977–5000.

Von Storch, H., Zwiers, F.W., 2002. Statistical analysis in climate research. Cambridge university press.

Wheeler, M.C., Hendon, H.H., 2004. An all-season real-time multivariate mjo index: Development of an index for monitoring and prediction. Monthly weather review 132, 1917–1932.

Wickham, H., 2016. ggplot2: elegant graphics for data analysis. springer.

Wilks, D.S., 2011. Statistical Methods in the Atmospheric Sciences. Academic Press. URL: http://books.google.com/books?hl=en{&}lr={&}id=IJuCVtQ0ySIC{&}pgis=1.

Álvarez, M.S., Vera, C.S., Kiladis, G.N., Liebmann, B., 2016. Influence of the madden julian oscillation on precipitation and surface air temperature in south america. Climate Dynamics 46, 245–262.

Monthly variations of forcing mechanisms of austral summer precipitation in subtropical Argentina

Santiago I. Hurtado: Conceptualization, Data Curation, Methodology, Software, Visualization, Formal analysis, Investigation, Writing - Original Draf, ; **Eduardo A. Agosta:** Investigation, Writing - Review & Editing, Supervision ; **Pablo G. Zaninelli:** Writing - Review & Editing, Supervision

Declaration of interests

☒The authors declare that they have no known competing financial interests or personal relationships that could have appeared to influence the work reported in this paper.

☐The authors declare the following financial interests/personal relationships which may be considered as potential competing interests:

Highlights

- December precipitation is mainly modulated by the ENSO.
- January precipitation is modulated by extratropical Rossby wave trains.
- February wet conditions over the south-west are linked to a Rossby wave in January.
- February wet conditions over the east are linked to an anomalous Walker cell.